Optimal Moth Eye Nanostructure Array on Transparent Glass Towards Broadband Antireflection

Seungmuk Ji,[†] Kyungjun Song,[†] Thanh Binh Nguyen,[†,‡] Namsoo Kim,[†] and Hyuneui Lim*,[†,‡]

[†]Department of Nature-Inspired Nanoconvergence Systems, Korea Institute of Machinery and Materials, 156 Gajeongbuk-Ro, Daejeon 305-343, Korea

[‡]Department of Nanobiotechnology, University of Science and Technology, 217 Gajeong-Ro, Daejeon 305-350, Korea

Ⓢ Supporting Information

ABSTRACT: Broadband antireflection (AR) is essential for improving the photocurrent generation of photovoltaic modules or the enhancement of visibility in optical devices. Beyond conventional AR coating methods, moth eye mimicking nanostructures give new directions to enhance broadband antireflection through the selection of geometrical parameters, such as height, periodic distance, shape, and arrangement. This study numerically and experimentally investigates the behavior of light on complex nanostructures designed to mimic the surface of the moth eye with mixed shapes and various arrangements. To obtain broadband AR, we rigorously study the design parameters, such as height, periodic distance, shape, and arrangement, on a transparent quartz substrate. Several kinds of nanopillar arrays are elaborately fabricated including mixed nanostructures comprising pointy and round shapes in ordered and random arrangements via colloidal lithography. The optimal morphology of moth eye nanostructure arrays for broadband antireflection is suggested in view of reflectance and average weight transmittance.

KEYWORDS: moth eye, broadband antireflection, nanostructures, mixed shape, arrangement, transparency
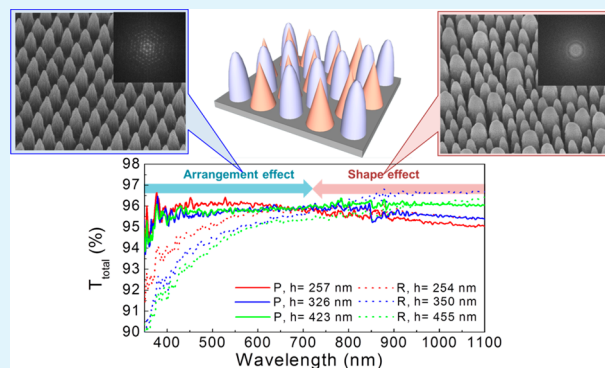
1. INTRODUCTION

Bioinspired nanostructures provide amazing multifunctional properties, such as hydrophilicity-based antifogging, super-hydrophobicity-based self-cleaning in combination with special optical properties, mechanical properties, adhesion properties, and so on.[1−8] These functions of nanostructures can lead to the innovative use of such technology in various industrial applications. Among them, nanostructures inspired by the corneal surface of the moth eye are the most promising structures with potential for commercialization in the near future.

The antireflective (AR) function of moth eyes exhibits exceptional broadband low reflectivity and high transmission with wide-angle incidence compared to conventional antireflective chemical coatings.[9−12] These bioinspired nanostructures are considered an effective means to enhance the photoconversion efficiency of solar cells[13−16] or the visibility of displays.[17]

Recently, numerous investigations have been carried out to realize an antireflective surface on silicon (Si) and glass substrates.[18−28] These studies have shown that broadband low AR behaviors can be controlled through the adjustment of structural design parameters, such as periodicity, height, shape, and arrangement. However, there have only been a couple of papers that have demonstrated broadband low AR properties on transparent substrates with structural design via numerical calculation. Structural randomness in position, diameter, and length of vertically aligned Si nanowires has been shown to enhance the absorption of light.[29,30] The broadband AR was demonstrated experimentally via dual-side nanotexturing with appropriate matching of nanopillar heights on quartz in our previous study.[24] A solar weighted average value over 99% was obtained for the range of 350−1100 nm owing to the broadband low reflectance values. However, in real application, AR structures on one side of the sample are generally required. Unfortunately, studies rarely examine complex nanostructures including mixed shapes and disordered arrangements because morphology control of the nanostructure on AR surfaces is difficult in fabrication.

Here, we demonstrate the antireflection and average weight transmittance of mixed shape and various arrangements of nanopillars on transparent quartz obtained by experiment and calculation. This study regarding optimal moth eye nanostructure arrays on transparent quartz was performed to achieve broadband antireflection and transmission.
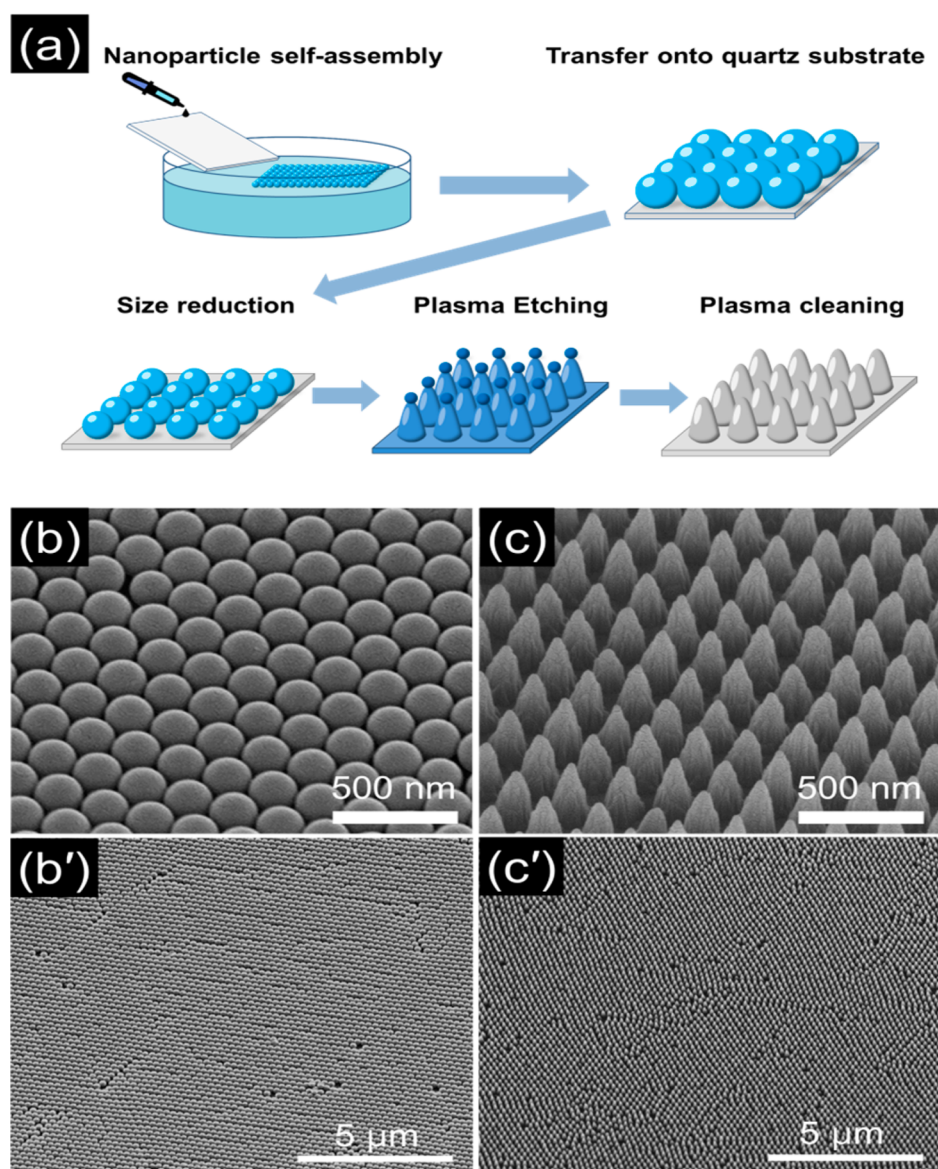
Figure 1. Fabrication process and FE-SEM images. (a) Schematic images of the fabrication process of moth-eye-mimicking nanostructures via colloidal lithography, (b) and (b′) FE-SEM image of PS nanoparticle array with high (×80 000) and low (×10 000) magnification, respectively, and (c) and (c′) FE-SEM images of moth eyes mimicking nanopillar arrays on quartz substrate with high (×80 000) and low (×10 000) magnification, respectively.

2. EXPERIMENTAL SECTION

2.1. Fabrication of Moth-Eye-Mimicking Nanostructures. A commercial polystyrene (PS) nanoparticle solution (Polyscience, Inc.) was used to make the periodic array of the mask. The concentration of the solution was 2.6%, and the size distributions of the solutions were 120 ± 7, 200 ± 10, and 356 ± 14 nm. Each nanoparticle solution was mixed with ethanol (Aldrich Inc.) in the proper ratio according to the nanoparticle size to control the solvent evaporation. As displayed in Figure 1(a), nanoparticle assembly was generated by dropping a few microliters of each prepared nanoparticle solution using a micropipet on the top of a hydrophilic supporting plate partially immersed in a deionized (DI) water bath. At three phase contact points, the nanoparticle assembly was floated on the water surface, and then some area of the assembly was picked up by using a 2.5 × 2.5 cm² quartz substrate.

For the random array, we mixed up two nanoparticle solutions having 200 ± 10 and 140 ± 10 nm diameter. Despite the difference in the size of the nanoparticles, closely packed nanoparticle arrays were formed on the air–water interface due to the nature of self-assembly.

Nanoparticles of 140 ± 10 nm in diameter were synthesized by an emulsifier-free polymerization method.

The plasma etching is performed to generate nanopillar arrays on the substrates coated with nanoparticles, by using a reactive ion etcher (RIE) (Miniplasma station, All For System). In the plasma etching process with spherical nanoparticles as a mask, the gap distance between neighboring nanoparticles is necessary to get the sites for the reaction between the quartz surface and plasma species. In this experiment, the gap distance was obtained with the level of size reduction of nanoparticles by 20% in O_2 plasma ambient. Subsequently, anisotropic etching was carried out in a mixture of CF_4, H_2, and O_2 gases with ratio of 2:3:0.1 with 150 W radio frequency power, and then the residuals and the remaining nanoparticles on the surface were removed by O_2 plasma treatment with power of 150 W for 3 min. The addition of O_2 gas during the anisotropic etching and final O_2 plasma cleaning with relative high power induced the size reduction of the nanoparticles and sharp apex on top of the nanopillars. Finally, the nanopillars having the pointy shape are formed as shown in Figure 1. The array of 200 nm nanoparticles and

the resulting nanopillar array after plasma etching are shown in Figure 1(b) and (c), respectively.

2.2. Characterizations. The surface morphology was characterized by field-emission scanning electron microscopy (FE-SEM) (Nova Nano SEM, FEI). The total transmittance and specular reflectance were measured by an UV-Vis-NIR spectrometer (U-4001, Hitachi) combined with an integrating sphere for the 350−1100 nm wavelength range.

2.3. Numerical Calculations. We conducted two types of calculations, namely, effective medium theory (EMT) and finite element method (FEM), by using Matlab (version 7.1, The MathWorks Inc.) and Comsol multiphysics (version 4.2, COMSOL Inc.), respectively. In EMT calculations, we describe the structural factors by the following equation[10]

$$r^* = \sqrt[\alpha]{p(1 - z^*)} \quad \alpha = 1: \text{pointy shape}, \quad \alpha = 2: \text{round shape}$$

(1)

where z^* and r^* are the relative coordinate of height and radius, respectively, and p is the ratio of the base radius to the distance between the pillars. We divided a nanopillar with 100 layers and calculated effective refractive index (n_e) of each layer by using the following formula[10]

$$n_e = (f(n_c)^{2/3} + (1 - f))^{3/2}, \quad f = \frac{2\pi r^{*2}}{\sqrt{3}}$$

(2)

where f is volume fraction of a nanopillar arranged hexagonally, and n_c is the refractive index of the substrate. Then, we achieved the values of transmittance or reflectance by solving the Fresnel's equations.

We ignored the light reflection of the back side of the substrates and only considered the 0th transmission and reflection because of the subwavelength elements ($\lambda \gg$ periodicity). Thus, EMT calculations were used to obtain the average weighted transmittance of the nanopillar arrays for 350−1100 nm. Although EMT calculations are favorable for fast and simple calculations compared to FEM calculations, EMT methods can only describe the effects of shape and aspect ratio of nanostructures in the long wavelength limit. Therefore, the overall optical response of moth eye nanostructures according to periodic distance, height, shape, as well as arrangement could be investigated by FEM calculations as presented in the Supporting Information.

3. RESULTS AND DISCUSSION

3.1. Effect of Periodic Distance and Height on Antireflection. Figure 1 shows a fabrication process of AR texturing and the resulting nanostructures on quartz substrate. We used a commercial polystyrene (PS) nanoparticle solution and a floating transfer method to make the mask of a periodic array of nanoparticles. Plasma etching was carried out to control the morphology of the nanopillars. In this study, two types of calculations, namely, effective medium theory (EMT) and the finite element method (FEM), were performed to predict the AR behavior of controlled structures of nanopillar arrays. EMT calculations are favorable for fast and simple calculations, and they can describe the effects of the shape and aspect ratio of nanostructures well.[10] FEM calculations are so delicate corresponding to several factors that the calculations were used to confirm the AR effect in relation to various design parameters, including periodic distance, height, shape, and arrangement in the Supporting Information.

The antireflection performance was observed on transparent quartz in relation to various periodic distances and heights of nanopillars. Figure 2(a) shows FE-SEM images of nanopillars which were fabricated by using PS nanoparticles of various sizes as a mask. The size of mask nanoparticles determines the periodic distance of nanopillar arrays. The particle sizes used in this study were 120 ± 7, 200 ± 10, and 356 ± 14 nm, and they
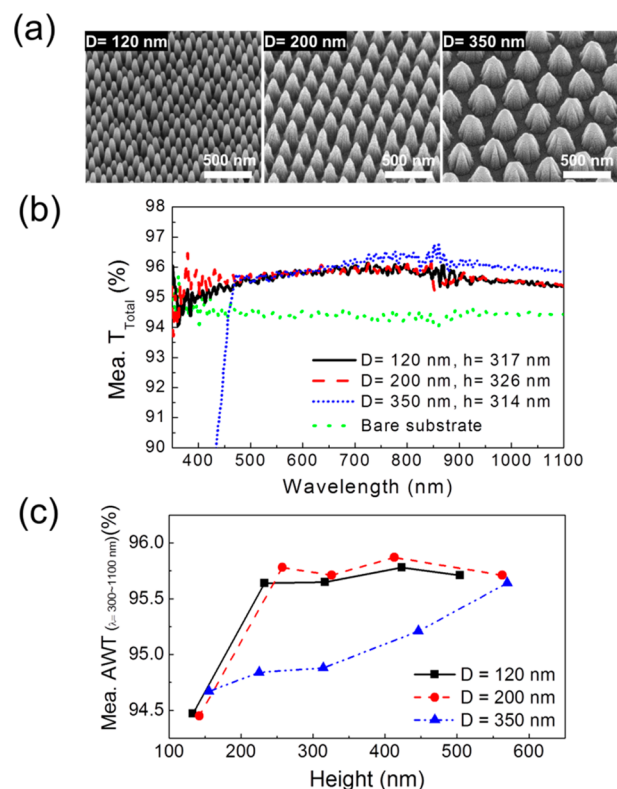
Figure 2. Surface morphologies and optical properties of moth eye nanostructures. (a) FE-SEM images with different periodic distances such as 120, 200, and 350 nm. (b) The measured total transmittance for around 320 nm in height. (c) The measured AWT values of nanopillar arrays having periodic distance of 120, 200, and 350 nm with different heights.

are denoted as D = 120, 200, and 350 nm, respectively (we use these notations in this paper for the description of periodicity). The total transmittance spectra corresponding to various periodic distances of nanopillar arrays with the height of 320 ± 19 nm and pointy shape are presented in Figure 2(b). While nanopillar arrays with D = 120 and 200 nm show similar spectra, the nanopillar array with D = 350 nm shows a high transmittance value at around 500 nm wavelength and a drastic drop below the wavelength of 470 nm. The drop of transmittance is attributed to light scattering due to a large period of nanopillars compared with the wavelength of incident light. However, nanopillars with D = 350 nm show slightly better antireflective behavior in the long wavelength range. These tendencies are also well established by the FEM simulations as shown in Figure S1 (Supporting Information). In these calculations, we used the height h = 320 nm and pointy shapes as illustrated in the inset of Figure S1 (Supporting Information).

To evaluate the antireflection performance of nanopillar arrays in solar cell application, we calculated the average weighted transmittance (AWT) over solar irradiance for 350−1100 nm wavelength. The AWT is given by

$$\text{AWT (\%)} = \frac{\int_{350nm}^{1100nm} T(\lambda) \times I(\lambda)_{AM1.5G} d\lambda}{\int_{350nm}^{1100nm} I(\lambda)_{AM1.5G} d\lambda}$$

(3)

where $T(\lambda)$ is the value of transmittance, and $I(\lambda)_{AM1.5G}$ is solar irradiance under the air mass (AM) condition of 1.5 G.[31] The
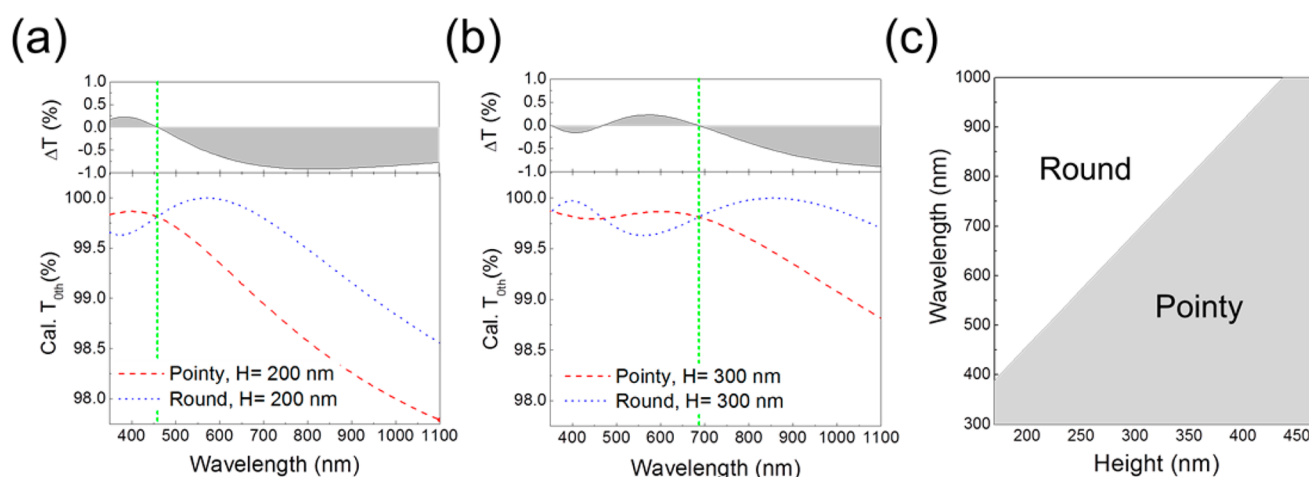
Figure 3. Calculated optical properties according to nanopillar shapes based on EMT. (a), (b) Calculated transmittance and difference in the transmittance of the pointy (red dashed line) and the round-shaped (blue dotted line) nanopillar array for 200 nm in diameter with 200 and 300 nm height, respectively. The crossing points are indicated by green dotted lines. (c) Expression of the crossing points corresponding to the height of nanopillars.
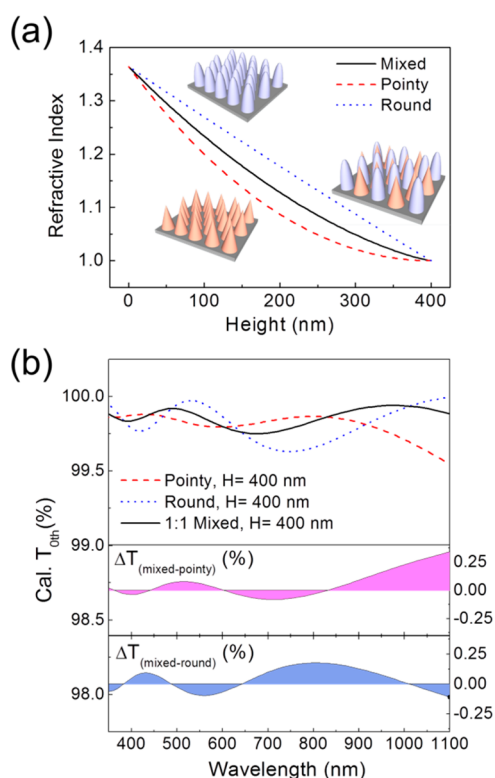

Figure 4. Refractive index profiles and transmittance spectra according to various shapes of nanopillar array for 400 nm in height based on EMT calculations. (a) Refractive index profiles of mixing, pointy, and round shaped nanopillar arrays are illustrated. (b) Transmittance spectra and relative differences in transmittance between mixed and other arrays. The graphs colored as pink and navy indicate the difference between mixed and pointy arrays $(\Delta T_{(\text{mixed-pointy})})$ and the difference between mixed and round arrays $(\Delta T_{(\text{mixed-round})})$, respectively.

results in Figure 2(c) clarify the effect of nanopillar height combined with the periodic distances of arrays. The nanopillar arrays with $D = 120$ nm or 200 nm showed similar AWT values for the 350−1100 nm wavelength range. Desirably, the measured AWT values of $D = 120$ and 200 nm were over

95.5% except in the case of height less than 150 nm. However, the nanopillar array with $D = 350$ nm showed low AWT values in the visible spectrum resulting from strong light scattering as observed in Figure 2(b).

For the nanopillar arrays of $D = 120$ and 200 nm, the maximum AWT values were obtained at a height around 400 nm. The nanopillar array with $D = 200$ nm exhibits transmission up to 95.9%. The decreasing of AWT of nanopillars over 400 nm in height is observed due to light scattering in the short wavelength region. Even though the nanopillar array with $D = 350$ nm shows continuously increasing AWT with increasing height, the further value of AWT is suppressed by multiple light scattering. Therefore, we suggest that efficient AR performance is obtained by nanopillars below $D = 200$ nm and around $h = 400$ nm for sunlight.

3.2. Effect of Shape on Antireflection. The AR behavior in relation to nanopillar shape was already dealt with in our previous study.[24] Experimentally, nanopillars with a sharp apex, such as a pointed cone, showed better antireflective properties than rounded cone or truncated cone shapes with a 500 nm height. To examine AR behavior in relation to nanopillar shape, we calculate the transmittance of two kinds of nanopillar arrays using an EMT method. Figure 3(a) and (b) displays the transmittance spectra of round and pointy-shaped nanopillars 200 nm in diameter with 200 and 300 nm height, respectively. The spectrum of round pillars crosses with that of pointy pillars at a certain wavelength. Experimentally, the crossing of spectra of two shapes was also observed in the measured spectra as seen in Figure S2 (Supporting Information). The upper part of Figure 3(a) and (b) shows the relative difference in transmission between the two spectra given by $\Delta T = T_{\text{Pointy}} - T_{\text{Round}}$; T_{Pointy} is the transmittance of arrays of pointy nanopillars, and T_{Round} is the transmittance of arrays of rounded nanopillars as a function of wavelength. The positive and negative area in these graphs shows the relatively superior transmission region of pointy and round-shaped nanopillars, respectively. Thus, in the left area of the crossing point indicated by the green dotted line, the array of pointy nanopillars outperforms the array of round nanopillars as indicated by positive ΔT. In contrast, the array of round nanopillars provides high transmittance compared to the array
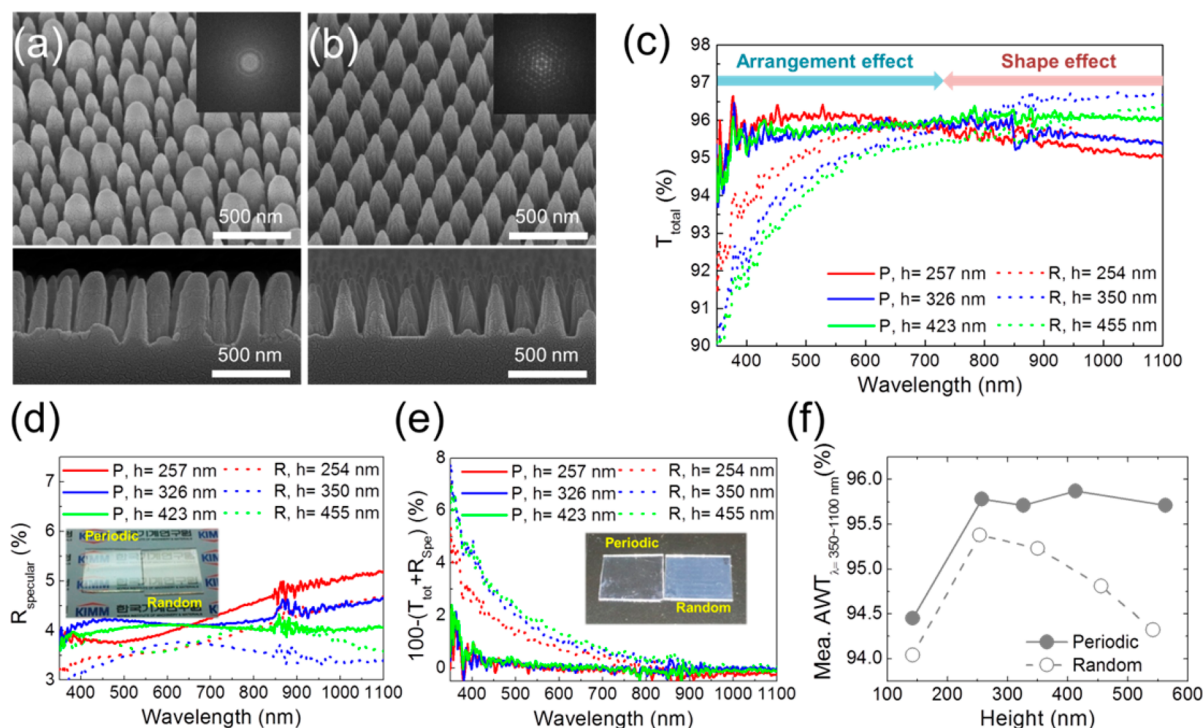
Figure 5. FE-SEM images and optical properties of the random arrays and the periodic arrays. (a) and (b) 30° tilted (top) and cross-sectional (bottom) FE-SEM images of a random mixed array and periodic pointy array, respectively. The inset shows the results of FFT analysis for two arrays. (c) The measured total transmittance, (d) specular reflectance, and (e) light scattering of fabricated surfaces. The light scattering can be inferred as $100 - (T + R)$, due to negligible absorption of the quartz substrate. The insets in (d) and (e) are photographic comparison of the two arrays with and without exposure of light source, respectively. (f) The measured AWT values of the random mixed arrays and periodic pointy arrays.

of pointy nanopillars in the right area of the crossing point. The crossing point linearly shifts to a longer wavelength as the nanopillar height increases as seen in Figure 3(c).

According to the upper results, we suppose that an array comprised of nanopillars with mixed shapes may improve the AR effect in the broadband wavelength range due to the advantages of both shapes. Theoretically, the refractive index (RI) profile of the mixed nanopillar array consisting of pointy and round shapes with a ratio of 1:1 was achieved by averaging the RI values of each shape corresponding to height. Figure 4(a) presents the RI profile of pointy, round, and mixed shapes for $h = 400$ nm. Interestingly, the mixed nanopillar array shows broadband enhancement in transmittance in comparison to the arrays of pointy or round nanopillars due to the reduction of fluctuating amplitude in Figure 4(b). The relative differences in transmittance between mixed and other arrays are compared in the bottom of Figure 4(b), showing that the mixed array has the overall higher transmittance than the other arrays. These tendencies were also verified by FEM methods as seen in Figure S3 (Supporting Information). Therefore, a mixture of nanopillar shapes achieves better AR performance than single shape nanopillars for the broad wavelength range.

3.3. Effect of Arrangement on Antireflection. The effects of arrangement on optical properties have not been studied much because it is very difficult to demonstrate the effect with experimental results. The arrangement of nano-structures has an influence on the AR effect because of different orientation of light scatterers. With regard to research on a-Si solar cells, the arrangement of nanostructures affects the guided mode coupling between the transparent conducting oxide and amorphous Si layer.[32,33] However, the replicate fluoropolymer

nipple arrays on glass substrates showed that the ordering did not play a crucial role in AR properties.[34]

To verify the effects of arrangement, we fabricated randomly arranged and comparatively ordered nanopillar arrays having fixed heights as shown in Figure 5(a) and (b), respectively. Unfortunately, the fabrication of nanopillar arrays having exactly different arrangements with the same morphology is not possible in our process. The mixture of different sized masking nanoparticles of 140 and 200 nm was used to give a random array on the surface. The randomness was confirmed by fast Fourier transform (FFT) analysis of FE-SEM images by using Image J (NIH) software. The random array showed no characteristic patterns in contrast with the periodic array as seen in the insets of Figure 5(a) and (b). When the etching duration is the same, the taper angle of the nanopillars is determined by the level of size reduction of masking nanoparticles in the process of colloidal lithography.[35] The size reduction of the random arrays is focused on the small particles, by reduction of 20% of 140 nm nanoparticles. Therefore, 200 nm nanoparticles produced a round shape, and 140 nm nanoparticles made the relatively pointy shapes in random arrays. The ordered sample had a pointy shape because it was only prepared with 200 nm nanoparticles.

The total transmittances of the randomly arranged and comparatively ordered nanopillar arrays were measured, and the results are shown in Figure 5(c). Spectra of the two kinds of arranged samples intersect in the wavelength range between 650 and 1000 nm. While the ordered samples showed improved transmittance at the short wavelength, the randomly arranged samples showed high values beyond the crossing point. In the reflection spectra, the random nanopillar array seemed to be less reflective than the periodic array under a

strong light source. This means that specular reflection is not dominant in a random array as shown in Figure 5(d). However, random mixed-shaped nanopillar arrays have a lower transmittance value than periodic pointy arrays below the crossing point. Declining transmittance in the short wavelength range in the random array is attributed to diffusive reflection as shown in Figure 5(e). Hence, the sample of random arrays is hazy, even though the specular reflectance is small.

The optical properties observed in Figure 5 result from the complex effects of the arrangement and shape of nanopillar arrays. The improvement of transmittance of the random array in the long wavelength region would be originated from the mixed shapes of nanopillars. This was confirmed by simulation via FEM as seen in Figure S4 (Supporting Information). The arrangement of nanopillars has little effect on transmittance beyond the crossing point, and there are some spikes in the short wavelength. Even though randomness of numerical calculations is limited by the unit cell size, the further increase of light scattering with random arrangement is explained by the spikes at the short wavelength. Therefore, it is supposed that transmission improvement beyond the crossing point is mainly due to mixed shape, mainly round nanopillars in the random array, and the effect of arrangement in the long wavelength range is small.

The AWT values of random arrays for each height are shown in Figure 5(f). The overall values of the random arrays were smaller than those of the periodic arrays. Above 200 nm in height, the AWT values of the random array decreased due to light scattering in the short wavelength regime. Therefore, we conclude that periodic nanopillar arrays are more effective for light transmission than random nanopillar arrays. The superiority of mixed arrays was verified by the transmittance improvement beyond the crossing point, but the overall transmittance was decreased by light scattering due to the random arrangement. If nanopillars are periodically arranged, broadband antireflection and transmission of mixed arrays will be fully demonstrated.

4. CONCLUSIONS

In summary, we demonstrated the efficient design of moth-eye-mimicking nanostructures for broadband antireflection performance. The effects of structural factors, such as height, periodic distance, shape, and arrangement, were investigated numerically and experimentally. Even though the highest transmission was observed from the nanopillar array higher than 350 nm, the size and period should be smaller than 200 nm to obtain the broadband antireflection effect due to the light scattering. The height of nanopillars around 400 nm with pointy shape is considered optimal for the best antireflection performance. Whereas random arrays showed lower specular reflectance than periodic arrays, random arrangement of nanopillars caused strong diffusive reflection at short wavelengths. The periodic nanostructure array provides better antireflection performance than the random array due to low light scattering. Furthermore, we suggest that the periodic array with nanopillars of mixed shapes is an efficient surface for broadband antireflection performance compared to arrays designed with nanopillars of a single shape.

ASSOCIATED CONTENT

Ⓢ Supporting Information
The calculated zeroth-order transmittance of nanopillar arrays based on FEM (finite element method) for different diameter, pointy and round shapes, and mixed shapes with various arrangements. This material is available free of charge via the Internet at http://pubs.acs.org.

AUTHOR INFORMATION

Corresponding Author
*Tel.: +82-42-868-7106. Fax: +82-42-868-7933. E-mail: helim@kimm.re.kr.

Notes
The authors declare no competing financial interest.

REFERENCES

(1) Park, K.; Choi, H. J.; Chang, C.; Cohen, R. E.; McKinley, G. H.; Barbastathis, G. ACS Nano 2012, 6, 3789−3799.
(2) Li, Y.; Zhang, J.; Zhu, S.; Dong, H.; Jia, F.; Wang, Z.; Sun, Z.; Zhang, L.; Li, Y.; Li, H.; Xu, W.; Yang, B. Adv. Mater. 2009, 21, 4731−4734.
(3) Leem, J. W.; Yu, J. S. Opt. Express 2012, 20, 26160−26166.
(4) Wisdom, K. M.; Watson, J. A.; Qua, X.; Liu, F.; Watson, G. S.; Chen, C.-H. Proc. Natl. Acad. Sci. U.S.A. 2013, 110, 7992−7997.
(5) Min, W.-L.; Jiang, B.; Jiang, P. Adv. Mater. 2008, 20, 3914−3918.
(6) Lim, H.; Jung, D.-H.; Noh, J.-H.; Choi, G.-R.; Kim, W.-D. Chin. Sci. Bull. 2009, 54, 3613−3616.
(7) Zheng, Y.; Gao, X.; Jiang, L. Soft Matter 2007, 3, 178−182.
(8) Lee, D. Y; Lee, D. H.; Lee, S. G.; Cho, K. Soft Matter 2012, 8, 4905−4910.
(9) Sun, C.-H.; Jiang, P.; Jiang, B. Appl. Phys. Lett. 2008, 92, 061112-1−3.
(10) Stavenga, D. G; Foletti, S.; Palasantzas, G.; Arikawa, K. Proc. R. Soc. London, Ser. B 2006, 273, 661−667.
(11) Huang, Y.-F.; Chattopadhyay, S.; Jen, Y.-J.; Peng, C.-Y.; Liu, T.-A.; Hsu, Y.-K.; Pan, C.-L.; Lo, H.-C.; Hsu, C.-H.; Chang, Y.-H.; Lee, C.-S.; Chen, K.-H.; Chen, L.-C. Nat. Nanotechnol. 2007, 2, 770−774.
(12) Päivänranta, B.; Saastamoinen, T.; Kuittinen, M. Nanotechnology 2009, 20, 375301.
(13) Yamada, N.; Ijiro, T.; Okamoto, E.; Hayashi, K.; Masuda, H. Opt. Express 2011, 19, A118−A125.
(14) Zhu, J.; Hsu, C.-M.; Yu, Z.; Fan, S.; Cui, Yi. Nano Lett. 2010, 10, 1979−1984.
(15) Chen, T.-G.; Yu, P.; Tsai, Y.-L.; Shen, C.-H.; Shieh, J.-M.; Tsai, M.-A.; Kuo, H.-C. Opt. Express 2012, 20, A412−A417.
(16) Kim, J.; Hong, A. J.; Nah, J.; Shin, B.; Ross, F. M.; Sadana, D. K. ACS Nano 2012, 6, 265−271.
(17) Taguchi, T.; Hayashi, H.; Fujii, A.; Tsuda, K.; Yamada, N.; Minoura, K.; Isurugi, A.; Ihara, I.; Itoh, Y. SID Int. Symp. Dig. Tech. Pap. 2010, 41, 1196−1199.
(18) Xu, H.; Lu, N.; Qi, D.; Hao, J.; Gao, L.; Zhang, B.; Chi, L. Small 2008, 4, 1972−1975.
(19) Boden, S. A.; Bagnall, D. M. Prog. Photovoltaics 2010, 18, 195−203.
(20) Boden, S. A.; Bagnall, D. M. Appl. Phys. Lett. 2008, 93, 133108-1−3.
(21) Li, Y.; Yu, H. Y.; Li, J.; Wong, S.-M.; Sun, X. W.; Li, X.; Cheng, C.; Fan, H. J.; Wang, J.; Singh, N.; Lo, P. G.-Q.; Kwong, D.-L. Small 2011, 7, 3138−3143.
(22) Chen, H. L.; Chuang, S. Y.; Lin, C. H.; Lin, Y. H. Opt. Express 2007, 15, 14793−14803.
(23) Zhu, J.; Yu, Z.; Burkhard, G. F.; Hsu, C.-M.; Connor, S. T.; Xu, Y.; Wang, Q.; McGehee, M.; Fan, S.; Cui, Y. Nano Lett. 2009, 9, 279−282.
(24) Ji, S.; Park, J.; Lim, H. Nanoscale 2012, 4, 4603−4610.

(25) Song, Y. M.; Choi, H. J.; Yu, J. S.; Lee, Y. T. *Opt. Express* **2010**, *18*, 13063−13071.

(26) Leem, J. W.; Yeh, Y.; Yu, J. S. *Opt. Express* **2012**, *20*, 4056−4066.

(27) Son, J.; Verma, L. K.; Danner, A. J.; Bhatia, C. S.; Yang, H. *Opt. Express* **2011**, *19*, A35−A40.

(28) Lohmüller, T.; Helgert, M.; Sundermann, M.; Brunner, R.; Spatz, J. P. *Nano Lett.* **2008**, *8*, 1429−1433.

(29) Du, Q. G.; Kam, C. H.; Demir, H. V.; Yu, H. Y.; Sun, X. W. *Opt. Lett.* **2011**, *36*, 1884−1886.

(30) Bao, H.; Ruan, X. *Opt. Lett.* **2010**, *35*, 3378−3380.

(31) The values of solar spectral irradiance are from the web site: http://rredc.nrel.gov/solar/spectra/am1.5/. (Accessed Aug 24, 2012).

(32) Battaglia, C.; Hsu, C.-M.; Söderström, K.; Escarré, J.; Haug, F.-J.; Charrière, M.; Boccard, M.; Despeisse, M.; Alexander, D. T. L.; Cantoni, M.; Cui, Y.; Ballif, C. *ACS Nano* **2012**, *6*, 2790−2797.

(33) Ferry, V. E.; Verschuuren, M. A.; van Lare, M. C.; Schropp, R. E. I.; Atwater, H. A.; Polman, A. *Nano Lett.* **2011**, *11*, 4239−4245.

(34) Sun, C.-H.; Gonzalez, A.; Linn, N. C.; Jiang, P.; Jiang, B. *Appl. Phys. Lett.* **2008**, *92*, 051107-1−3.

(35) Hsu, C.-M.; Connor, S.T.; Tang, M. X.; Cui, Y. *Appl. Phys. Lett.* **2008**, *93*, 133109-1−3.